Pulished in Nature Physics **16**, 526 (2020)

# Proximity-induced superconducting gap in the quantum spin Hall edge state of monolayer $WTe_2$

Felix Lüpke,[1,*] Dacen Waters,[1,*] Sergio C. de la Barrera,[1] Michael Widom,[1] David G. Mandrus,[2,3,4] Jiaqiang Yan,[2] Randall M. Feenstra,[1] and Benjamin M. Hunt[1,†]

[1]*Department of Physics, Carnegie Mellon University, Pittsburgh, PA 15213*
[2]*Materials Science and Technology Division, Oak Ridge National Laboratory, Oak Ridge, TN 37831, USA*
[3]*Department of Materials Science and Engineering, University of Tennessee, Knoxville, TN 37996, USA*
[4]*Department of Physics and Astronomy, University of Tennessee, Knoxville, TN 37996, USA*

**The quantum spin Hall (QSH) state was recently demonstrated in monolayers of the transition metal dichalcogenide 1T'-$WTe_2$ and is characterized by a band gap in the two-dimensional (2D) interior and helical one-dimensional (1D) edge states [1–3]. Inducing superconductivity in the helical edge states would result in a 1D topological superconductor, a highly sought-after state of matter [4]. In the present study, we use a novel dry-transfer flip technique to place atomically-thin layers of $WTe_2$ on a van der Waals superconductor, $NbSe_2$. Using scanning tunneling microscopy and spectroscopy (STM/STS), we demonstrate atomically clean surfaces and interfaces and the presence of a proximity-induced superconducting gap in the $WTe_2$ for thicknesses from a monolayer up to 7 crystalline layers. At the edge of the $WTe_2$ monolayer, we show that the superconducting gap coexists with the characteristic spectroscopic signature of the QSH edge state. Taken together, these observations provide conclusive evidence for proximity-induced superconductivity in the QSH edge state in $WTe_2$, a crucial step towards realizing 1D topological superconductivity in this van der Waals material platform.**

A topological superconductor is a state of matter classified by a pairing gap that gives rise to protected gapless excitations at its boundaries. Contemporary interest in topological superconductors has been driven by these gapless excitations, thought to be emergent Majorana quasiparticles with non-abelian statistics [5–8]. One path toward topological superconductivity is to realize an intrinsic spinless $p$-wave superconductor [9]. A powerful alternative is by using a conventional $s$-wave superconductor to induce Cooper pairing in topologically non-trivial states via the superconducting proximity effect, resulting in an effective $p$-wave pairing [10]. This approach has been employed to engineer 2D topological superconductivity in epitaxial topological insulator films grown on a superconducting substrate [11, 12], and 1D topological superconductivity by proximitizing a quantum spin Hall (QSH) state in buried epitaxial semiconductor quantum wells [13, 14]. While such demonstrations mark important milestones, there are clear advantages for exploring topological superconductivity in the van der Waals material platform. Using layered 2D materials allows the 2D QSH edge to be proximitized in vertical heterostructures, circumventing the length restrictions of lateral proximity-effect geometries. Furthermore, the surfaces and edges are readily available for surface probes, allowing detection and fundamental study of signatures of the topological superconducting state.

Following recent theoretical predictions [15], an intrinsic QSH state was demonstrated in a monolayer (ML) of 1T'-$WTe_2$ [1–3, 16–18]. $WTe_2$ is attractive for studying the QSH edge modes because it can be readily incorporated in van der Waals heterostructures and has shown quantized edge conductance up to 100 K [3]. Furthermore, ML $WTe_2$ was recently also shown to host intrinsic superconducting behavior below $\sim$1 K when electrostatically gated into the conduction band [19, 20].

In the present work, we study mechanically-exfoliated single- and few-layers of $WTe_2$ which have been transferred onto a van der Waals $s$-wave superconductor, $NbSe_2$. We show that this approach induces a superconducting gap in the $WTe_2$ without the need for electrostatic doping and yields a critical temperature much higher than that of the intrinsic $WTe_2$ superconductivity, an experimental advantage which greatly facilitates studies of the interplay of superconductivity and the QSH edge modes. We employ scanning tunneling microscopy and spectroscopy (STM/STS) to investigate the proximity-induced superconducting gap as a function of temperature, magnetic field, and $WTe_2$ thickness. By spatially resolving the spectroscopic features of the $WTe_2$, we find that the superconducting gap coexists with the QSH signature at the ML $WTe_2$ edge, demonstrating critical steps toward identifying 1D topological superconductivity in a van der Waals material system.

We have developed a novel fabrication technique which enables the assembly and deterministic placement of van der Waals heterostructures (Fig. 1a). Though similar methods have been used to fabricate complex encapsulated mesoscale devices [21], critically, our technique produces atomically-clean surfaces of air-sensitive materials suitable for scanning probe measurements. Figure 1b shows an STM image of a heterostructure where the $WTe_2$ ML edge and the underlying $NbSe_2$ are visible, showing atomically-clean surfaces on each material. The height profile across the step edge gives a step height of $\sim$7 Å which corresponds to one $WTe_2$ layer [17], indicating an atomically-clean interface between the $WTe_2$ and $NbSe_2$. Atomically-resolved STM images of the $NbSe_2$ surface (Fig. 1c) show the well-known $3 \times 3$ charge density wave [11], indicating the pristine quality of the $NbSe_2$ substrate. Atomically-resolved STM images of the $WTe_2$ ML (Fig. 1d) are characterized by vertical atomic rows parallel to the $b$-axis

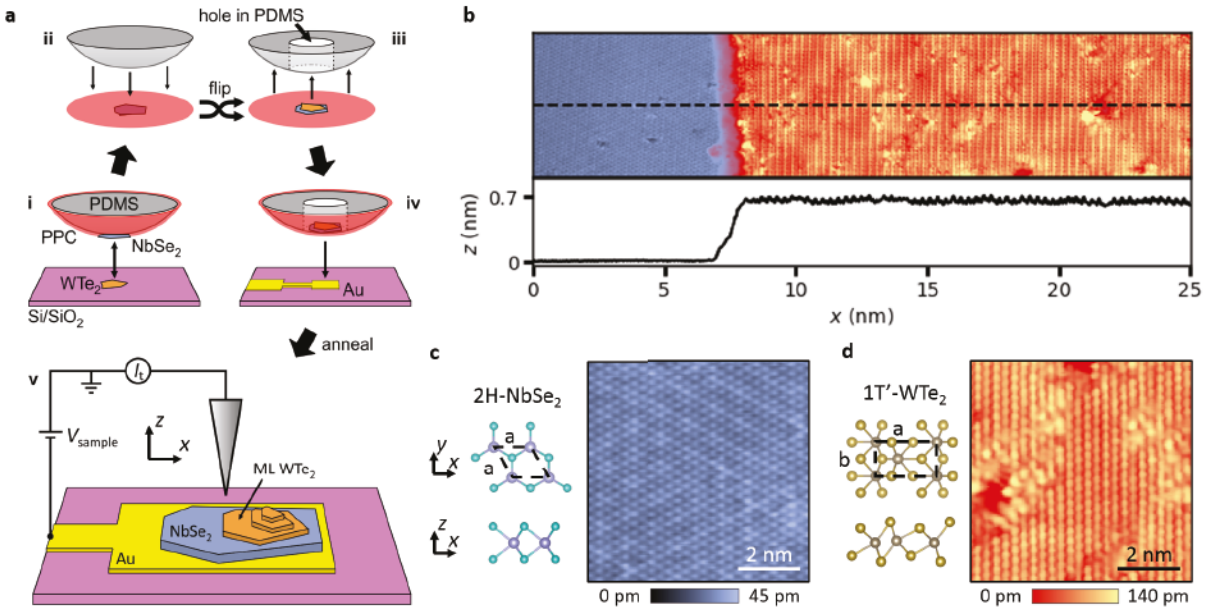


FIG. 1. **Fabrication and morphology of $WTe_2$/$NbSe_2$ heterostructure.** **(a)** Schematic of the sample fabrication. After assembly of the $NbSe_2$/$WTe_2$ heterostructure using a PPC/PDMS stamp (inside a nitrogen-filled glove box), the PPC film is peeled off, flipped upside down and put onto a new PDMS stamp which has a hole in it. This stamp is used to deterministically place the heterostructure onto pre-patterned gold leads without bringing the heterostructure surface into contact with any polymers or solvents. The PPC is then evaporated by annealing under vacuum conditions and the sample is transferred to the STM, all without intermediate air-exposure. **(b)** STM topography and height profile across the edge of the monolayer $WTe_2$ flake ($V_{\mathrm{sample}} = 300\,\mathrm{mV}$ and $I_{\mathrm{t}} = 10\,\mathrm{pA}$). **(c)** Atomic structures and atomically-resolved STM image of the $NbSe_2$ flake showing the $3 \times 3$ CDW ($V_{\mathrm{sample}} = 300\,\mathrm{mV}$ and $I_{\mathrm{t}} = 35\,\mathrm{pA}$). **(d)** Atomic structures and atomically-resolved STM image of ML $WTe_2$ ($V_{\mathrm{sample}} = 1\,\mathrm{V}$ and $I_{\mathrm{t}} = 55\,\mathrm{pA}$). In (b) a moiré pattern in the form of diagonal stripes can be seen on the ML $WTe_2$ resulting from the superposition of the two different atomic lattices. While $NbSe_2$ has a hexagonal unit cell with lattice parameters $a = b = 3.44\,\mathrm{Å}$, $WTe_2$ has a rectangular unit cell with lattice parameters $a = 6.28\,\mathrm{Å}$ and $b = 3.48\,\mathrm{Å}$ (Fig. 1c, d). The moiré pattern, analyzed in more detail in the SI, corresponds to a twist angle of $\approx 3°$. The topographies shown in (b), (c), and (d) are representative of the heterostructure over most of the area of the exfoliated flakes.

of the $WTe_2$ unit cell. Turning now to spectroscopic analysis of these surfaces, Fig. 2a shows a map of $dI/dV$ spectra taken along a line perpendicular to the $WTe_2$ monolayer step edge (upper panel) and the corresponding height profile (lower panel). The $dI/dV$ spectra clearly show the presence of an increased local density of states (LDOS) near the $WTe_2$ step edge. This feature was recently reported in STM/STS studies of ML films of $WTe_2$ grown on epitaxial graphene substrates [1, 16]. Based on combined evidence from ARPES and STS in Ref. 1, it was concluded that ML $WTe_2$ has a band gap of $(56 \pm 14)\,\mathrm{meV}$, and that the increased LDOS at the ML $WTe_2$ edge signifies the metallic QSH edge state. In our monolayer samples, produced via isolation from bulk crystals rather than molecular beam epitaxy, and on superconducting substrates rather than graphene, we observe the same spectroscopic features, which we attribute to the same QSH edge state. Figure 2b shows the averaged $dI/dV$ spectrum on the $WTe_2$ ML (red) and the ML edge (orange) at the corresponding positions indicated in Fig. 2a. The spectroscopic signature of the QSH edge state is evident primarily in the valence band but, importantly, the edge state also crosses the band gap. Following the interpretation of Ref. 1, the increases in the $dI/dV$ signal at $E - E_{\mathrm{F}} \approx -50\,\mathrm{meV}$ and $E - E_{\mathrm{F}} \approx 15\,\mathrm{meV}$ correspond to the onset of the $WTe_2$ valence and conduction band, respectively, locating $E_F$ in the ML $WTe_2$ band gap. A non-zero $dI/dV$ signal in the band gap away from the step edge was proposed to be due to defect states and substrate effects [1]. In addition, tip-induced band bending may play a role in introducing spectral weight in the $WTe_2$ band gap (see Supplementary Information (SI)). By comparing the positions of the observed spectral features to epitaxially-grown $WTe_2$ on graphene [1, 16] and exfoliated $WTe_2$ [22], we conclude that there is no significant charge transfer from the $NbSe_2$ to the $WTe_2$. This observation is further supported by our density functional theory (DFT) calculations of the ML $WTe_2$/$NbSe_2$ heterostructure, which show no significant modification of the $WTe_2$ electronic structure compared to a freestanding ML of $WTe_2$ (see SI).

Measurements of the ML $WTe_2$ $dI/dV$ spectrum over a smaller voltage range (Fig. 2c), reveal a new feature: a superconducting gap-like feature centered around the Fermi energy, characterized by a dip in the $dI/dV$ signal with peaks on either side of the gap. Comparison of measurements at 4.7 K and 2.8 K show that the gap deepens and the peaks sharpen at lower temperature. The evolution of the superconducting gap-like feature under application of a surface-normal mag-

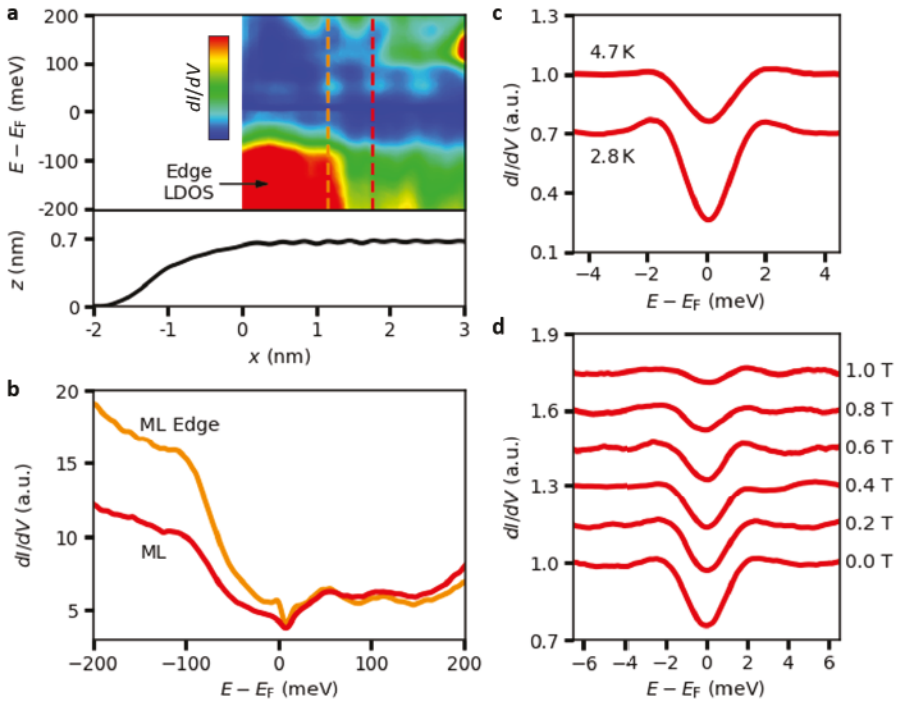


FIG. 2. **Simultaneous presence of quantum spin Hall edge state and superconducting gap in monolayer $WTe_2$.** **(a)** $dI/dV$ spectra taken along a line across the step edge of the $WTe_2$ flake (top), and corresponding height profile (bottom) ($V_{\mathrm{sample}} = 300\,\mathrm{mV}$ and $I_t = 400\,\mathrm{pA}$). **(b)** Spatially averaged $dI/dV$ spectra of monolayer $WTe_2$ showing a representative spectrum away from the monolayer edge (corresponding to the red dashed line in a)) and increased density of states at the monolayer edge due to presence of the QSH edge state (corresponding to orange dashed line in a)). Small voltage range $dI/dV$ spectrum of monolayer $WTe_2$ at 4.7 K and 2.8 K showing superconducting gap-like features. The 2.8 K curve is offset for clarity. **(d)** Magnetic field dependence of the small voltage spectrum of monolayer $WTe_2$ measured at 4.7 K. The curves are offset for clarity.

netic field at 4.7 K (Fig. 2d) shows that with increasing magnetic field, the gap becomes less deep and the peaks flatten out until the gap features have nearly vanished at 1 T. To understand this gap, we fit the observed superconducting-like gap with the Bardeen-Cooper-Schrieffer (BCS) spectrum (see SI). We find that the BCS model fits both the monolayer $WTe_2$ and the $NbSe_2$ data well (Fig. 3a). For $NbSe_2$, the fit results in a superconducting gap of $\Delta_{NbSe_2} = (0.84 \pm 0.01)\,\mathrm{meV}$, while for the $WTe_2$ it results $\Delta_{WTe_2} = (0.72 \pm 0.02)\,\mathrm{meV}$. In addition to following the trend of a superconducting gap with applied magnetic field, the vanishing of the gap near 1 T also agrees with the Ginzburg-Landau estimate for the upper critical field of bulk $NbSe_2$ [23]. We conclude that the gap feature observed on the ML $WTe_2$ is indeed a superconducting gap.

In order to confirm the proximity-induced nature of the observed superconducting gap, we explore its evolution as a function of $WTe_2$ thickness. The exfoliation procedure naturally produces terraces of varying thickness in our samples, enabling thickness-dependent gap measurement within a single sample. Figure 3b shows the superconducting gap measured on terraces of different numbers of $WTe_2$ layers $N$, revealing that the gap decreases with increasing $N$, as expected for decaying superconducting correlations near the boundary of a superconducting–metal interface [24]. To quantify this behavior, we fit the BCS model to each of the spectra in Fig. 3b and plot the extracted gap sizes as filled circles in Fig. 3c. In the thick limit ($N \geq 3$), we find that observed behavior shows excellent agreement with transport measurements of proximity-induced superconductivity in bulk $WTe_2$ flakes [24, 25], extending the previous studies to the ultra-thin limit (see SI). For $N < 3$, we observe a more rapid decrease of the extracted gap which may be explained by the strong dependence of the electronic structure of the $WTe_2$ in this thickness range, resulting in a larger mismatch of the $WTe_2$ and $NbSe_2$ Fermi surfaces and therefore a stronger dependence of the induced gap on $N$ [26].

For monolayer and bilayer $WTe_2/NbSe_2$, we also consider the possibility that the spectra may be a superposition of tunneling into $WTe_2$ and into $NbSe_2$ (Fig. 4a,b inset). We therefore performed a control experiment, tunneling into ML $WTe_2$ on a ∼20 nm thick hBN substrate, in order to isolate the relative contributions (Fig. 4a,b). This allows us to perform a more detailed analysis of the ML $WTe_2$ /$NbSe_2$ spectrum (Fig. 4d) in which we fit a superposition of BCS spectra, with a 14% fractional contribution from ML $WTe_2$ . The resulting induced gap size is $\Delta^{(ML)}_{WTe_2} = 0.76 \pm 0.16$ meV at 4.7 K and $0.83 \pm 0.08$ meV at 2.8 K (Fig. 4d). For the bilayer, we find a fractional contribution of 75% and an induced gap

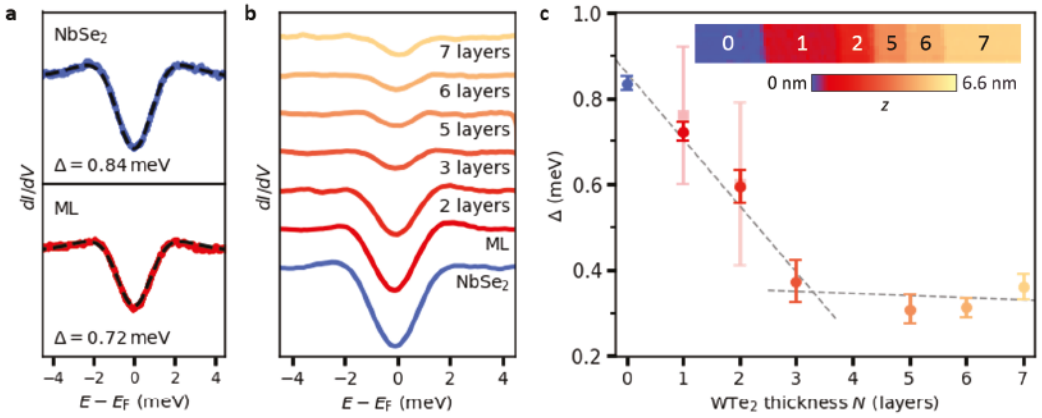


FIG. 3. **Evolution of the superconducting gap with $WTe_2$ thickness at 4.7 K.** **(a)** Fits of the BCS model to the superconducting gap spectra measured on $NbSe_2$ and monolayer $WTe_2$ result in $\Delta_{NbSe_2} = (0.84 \pm 0.01)$ meV and $\Delta_{WTe_2} = (0.72 \pm 0.02)$ meV. **(b)** Measurement of the superconducting gap spectrum for $WTe_2$ layer thicknesses up to 7 layers. **(c)** (filled circles) $WTe_2$ thickness dependence of the superconducting gap size obtained from fitting the spectra in (b) with the BCS gap equation. (filled squares) Fits of the monolayer and bilayer spectrum with a more detailed model which includes partial tunneling into the $NbSe_2$ substrate. The dashed lines indicate two different regimes in which $\Delta$ decreases more rapidly for $N < 3$ and more gradually for $N \geq 3$. The inset shows a large-scale topography image of the $WTe_2$, where terraces of different $WTe_2$ thicknesses are observed. Scan size: 200 nm × 14 nm. The corresponding number of $WTe_2$ layers $N$ is indicated for each terrace, where $N = 0$ is the bare $NbSe_2$.

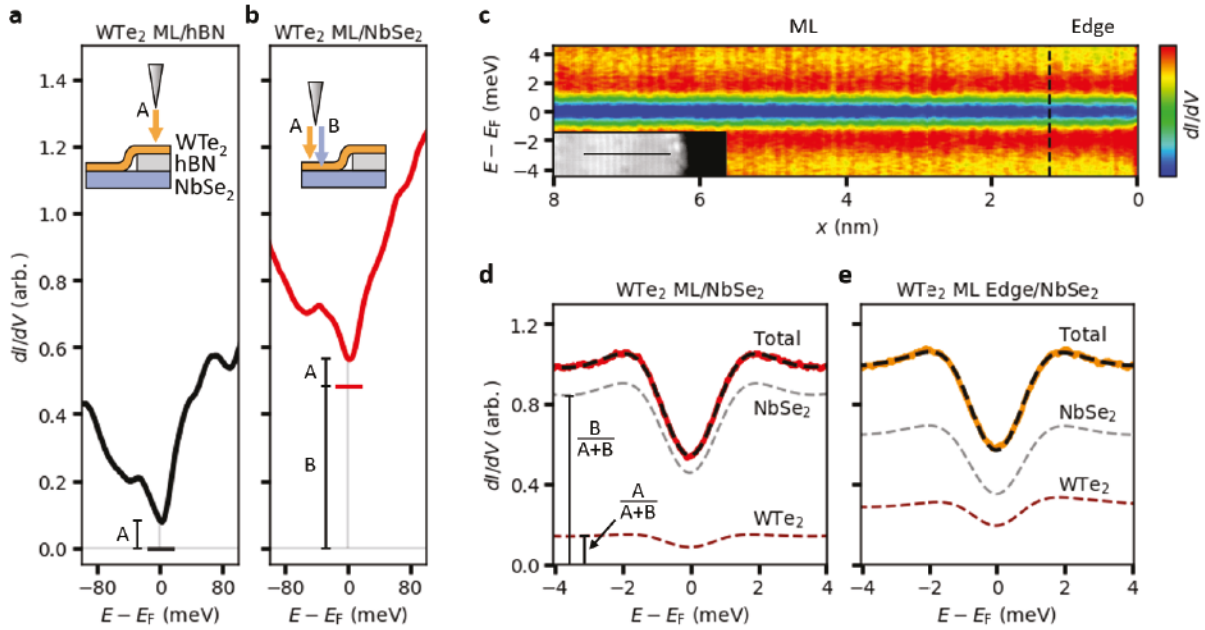


FIG. 4. **Proximity-induced superconducting gap in the quantum spin Hall edge state of monolayer $WTe_2$ at 2.8 K.** **(a)** Tunneling spectrum of $WTe_2$ on hexagonal boron nitride (hBN) and **(b)** spectrum of the *same* $WTe_2$ flake on $NbSe_2$ (for optical micrograph of the heterostructure see SI). The tunneling contributions of the $WTe_2$ and $NbSe_2$ are indicated as $A$ and $B$, respectively. **(c)** SC gap spectra measured along a line perpendicular to the edge of the $WTe_2$. The inset shows the topography and line along which the spectra were taken. Scan size: 16 nm × 4 nm. **(d)** Fitting of representative ML $WTe_2/NbSe_2$ tunneling spectrum. The fractional contribution of tunneling into $WTe_2$ is $f_{WTe_2} \equiv A/(A+B) = 0.14 \pm 0.04$. The $NbSe_2$-derived states contribution is therefore $f_{NbSe_2} = B/(A+B) = 0.86 \pm 0.04$. The model used to fit the data is $(dI/dV)_{\text{Total}} = f_{WTe_2} \cdot (dI/dV)_{WTe_2} + f_{NbSe_2} \cdot (dI/dV)_{NbSe_2}$, using a BCS form for each $dI/dV$ (details in SI). The grey and maroon dashed lines indicate the $(dI/dV)_{NbSe_2}$ and $(dI/dV)_{WTe_2}$, the proximity-induced SC gap in the $WTe_2$. The size of the induced gap is $\Delta^{(ML)}_{WTe_2} = 0.83 \pm 0.08$ meV. **(e)** Fitting of the ML edge $WTe_2/NbSe_2$ tunneling spectrum. We use the same gap(s) found for $NbSe_2$ from (a) and use $\Delta^{(edge)}_{WTe_2}$ and the new fractional contribution of the $WTe_2$ edge state, $f^{(edge)}_{WTe_2}$ as fitting parameters (details in SI). The resulting induced SC gap in the $WTe_2$ QSH edge state is $\Delta^{(edge)}_{WTe_2} = 0.75 \pm 0.08$ meV.

of $\Delta_{WTe_2}^{(BL)} = 0.60 \pm 0.19$ meV. In Fig. 3c we plot the 4.7 K induced gaps and find no significant deviation from those determined by the one-gap fits.

Finally, we consider the lateral variation of the superconducting gap from within the ML $WTe_2$ to the region occupied by the edge state. Figure 4c shows $dI/dV$ spectra taken at 2.8 K along a line approaching the physical edge of the $WTe_2$ monolayer, similar to that shown in Fig. 2a but over a smaller voltage range. The superconducting gap is present throughout the $WTe_2$ monolayer with only slight changes in the gap width and depth. It is apparent that a superconducting gap is present in the region in which the QSH edge state is observed in Fig. 2a (indicated by the dashed line in Fig. 4c). To confirm that there is a fractional contribution to this spectrum due to an induced gap in the QSH edge state, in Fig. 4e we perform a similar fit as we did for the spectrum 10 nm away from the edge in Fig. 4d. We find that the induced gap in the edge state has a value of $\Delta_{WTe_2}^{(edge)} = 0.75 \pm 0.08$ meV. The observation of a gap in the edge state of monolayer 1T'-$WTe_2$ provides strong evidence that we have created a 1D topological insulator in a van der Waals heterostructure by proximity-induced superconductivity in the quantum spin Hall edge state.

The topological nature of a superconducting QSH edge state could be explicitly demonstrated in an STM measurement by creating a boundary with a portion of the same QSH edge state in which a topologically-trivial gap has been opened [4]. This would localize Majorana zero modes at the boundary, which can be identified as a zero-bias conductance peak within the superconducting gap [27]. Creating such a boundary is straightforward in the van der Waals material platform, e.g., by integrating a van der Waals magnetic insulator into the heterostructure shown in Fig. 1a to open a local Zeeman gap. Our work establishes the groundwork for such an experiment with a clear path toward the realization of Majorana quasiparticles. In addition, the method of sample preparation outlined in this work may be easily adapted to numerous experiments involving surface-probe studies or air-sensitive materials.

## METHODS

$WTe_2$ and $NbSe_2$ were exfoliated onto $SiO_2$ in a nitrogen-filled glovebox. A $WTe_2$ flake with regions of different thicknesses was transferred onto a $(20 \pm 1)$ nm thick $NbSe_2$ flake using the technique depicted in Fig. 1a. At this thickness, the electronic properties of the $NbSe_2$ are bulk-like and the critical temperature below which the $NbSe_2$ becomes superconducting is $T_c \approx 7$ K [28]. For optical images of the sample and further details on the sample fabrication see SI. The STM tip is approached to the $WTe_2/NbSe_2$ heterostructure using a capacitive technique adapted from Ref. [29]. The commercial CreaTec STM helium bath temperature is 4.2 K with the ability of intermittently reaching $\sim 1$ K by pumping on the cryostat. The resulting STM temperatures are 4.7 K and 2.8 K, respectively, due to vibration isolation and optical access. The STM is equipped with an electrochemically-etched tungsten tip which was indented into gold prior to and in between measurements. The lock-in frequency was set to $f = 925$ Hz in all $dI/dV$ measurements. All superconducting gap measurements were performed at $V_{sample} = 5$ mV with $V_{mod} = 100\,\mu$V peak-to-peak and $I_t = 100$ pA, except in Fig. 2 e) where $V_{sample} = 10$ mV. The spectra in Fig. 2 a) and b) were acquired using $V_{mod} = 5$ mV. In Fig. 4, tunneling parameters are: $V_{sample} = 300$ mV, $I_t = 100$ pA and $V_{mod} = 5$ mV in (a) and $V_{sample} = 300$ mV, $I_t = 110$ pA and $V_{mod} = 10$ mV in (b). For quantitative comparison, the two spectra were normalized to the tunneling current and $V_{mod}$.

## ACKNOWLEDGMENTS

The authors acknowledge Di Xiao, David Cobden and Xiaodong Xu for helpful discussions and Nicholas Speeney and Nicolas Iskos for assistance in the lab. B.M.H. was supported by the Department of Energy under the Early Career award program (#DE-SC0018115). Crystal growth and characterization at ORNL was supported by the US Department of Energy, Office of Science, Basic Energy Sciences, Division of Materials Sciences and Engineering. The authors thank the Pennsylvania State University Two-Dimensional Crystal Consortium - Materials Innovation Platform (2DCC-MIP) which is supported by NSF DMR-1539916 for supplying further 2D materials. F.L. and D.W. were supported by the NSF DMR-1809145) for the STM measurements. The authors gratefully acknowledge NSF DMR-1626099 for acquisition of the STM instrument. S.C.d.l.B. was supported by the Department of Energy (#DE-SC0018115) for fabrication of proximity-effect van der Waals heterostructures. DFT Calculations were supported by the DOE under grant #DE-SC0014506.

## AUTHOR CONTRIBUTIONS

F.L., D.W., R.M.F. and B.M.H. designed the experiment. F.L. and D.W. acquired the experimental data and F.L., D.W., and R.M.F. analyzed the data and performed the fitting to the spectra. F.L., D.W. and S.C.d.l.B. fabricated the samples. F.L., D.W., S.C.d.l.B. and B.M.H. wrote the manuscript, and all authors commented on the manuscript. J.Y. grew the $WTe_2$ crystals. D.M. provided other van der Waals crystals used in this study. M.W. performed DFT calculations. R.M.F. and B.M.H. supervised the project.

* These authors contributed equally.
† bmhunt@andrew.cmu.edu

[1] Tang, S. *et al.* Quantum spin Hall state in monolayer $1T'$ – $WTe_2$. *Nat. Phys.* **13**, 683 (2017).

[2] Fei, Z. *et al.* Edge conduction in monolayer $WTe_2$. *Nat. Phys.* **13**, 677 (2017).

[3] Wu, S. *et al.* Observation of the quantum spin Hall effect up to 100 Kelvin in a monolayer crystal. *Science* **359**, 76–79 (2018).

[4] Alicea, J. New directions in the pursuit of Majorana fermions in solid state systems. *Rep. Prog. Phys.* **75**, 076501 (2012).

[5] Kitaev, A. Y. Unpaired Majorana fermions in quantum wires. *Phys.-Uspekhi* **44**, 131–136 (2001).

[6] Fu, L. & Kane, C. L. Superconducting proximity effect and Majorana fermions at the surface of a topological insulator. *Phys. Rev. Lett.* **100**, 096407 (2008).

[7] Sarma, S. D., Freedman, M. & Nayak, C. Majorana zero modes and topological quantum computation. *npj Quantum Inf.* **1**, 15001 (2015).

[8] Sato, M. & Ando, Y. Topological superconductors: a review. *Rep. Prog. Phys.* **80**, 076501 (2017).

[9] Maeno, Y., Kittaka, S., Nomura, T., Yonezawa, S. & Ishida, K. Evaluation of spin-triplet superconductivity in $Sr_2RuO_4$. *J. Phys. Soc. Jpn.* **81**, 011009 (2012).

[10] Fu, L. & Kane, C. L. Josephson current and noise at a superconductor/quantum-spin-Hall-insulator/superconductor junction. *Phys. Rev. B* **79**, 161408 (2009).

[11] Wang, M.-X. *et al.* The coexistence of superconductivity and topological order in the $Bi_2Se_3$ thin films. *Science* **336**, 52–55 (2012).

[12] Sun, H.-H. *et al.* Majorana zero mode detected with spin selective Andreev reflection in the vortex of a topological superconductor. *Phys. Rev. Lett.* **116**, 257003 (2016).

[13] Hart, S. *et al.* Induced superconductivity in the quantum spin Hall edge. *Nat. Phys.* **10**, 638–643 (2014).

[14] Bocquillon, E. *et al.* Gapless Andreev bound states in the quantum spin Hall insulator HgTe. *Nat. Nanotechnol.* **12**, 137 (2016).

[15] Qian, X., Liu, J., Fu, L. & Li, J. Quantum spin Hall effect in two-dimensional transition metal dichalcogenides. *Science* **346**, 1344–1347 (2014).

[16] Jia, Z.-Y. *et al.* Direct visualization of a two-dimensional topological insulator in the single-layer $1T^{'} - WTe_2$. *Phys. Rev. B* **96**, 041108 (2017).

[17] Peng, L. *et al.* Observation of topological states residing at step edges of $WTe_2$. *Nat. Commun.* **8**, 659 (2017).

[18] Shi, Y. *et al.* Imaging quantum spin Hall edges in monolayer $WTe_2$. *Sci. Adv.* **5** (2019).

[19] Fatemi, V. *et al.* Electrically tunable low-density superconductivity in a monolayer topological insulator. *Science* **362**, 926 (2018).

[20] Sajadi, E. *et al.* Gate-induced superconductivity in a monolayer topological insulator. *Science* **362**, 922 (2018).

[21] Zeng, Y. *et al.* High-quality magnetotransport in graphene using the edge-free Corbino geometry. *Phys. Rev. Lett.* **122**, 137701 (2019).

[22] Cucchi, I. *et al.* Microfocus laserangle-resolved photoemission on encapsulated mono-, bi-, and few-layer $1T^{'} - WTe_2$. *Nano Lett.* **19**, 554–560 (2019).

[23] Garoche, P., Veyssi, J. J., Manuel, P. & Molini, P. Experimental investigation of superconductivity in 2H-$NbSe_2$ single crystal. *Solid State Commun.* **19**, 455–460 (1976).

[24] Huang, C. *et al.* Inducing strong superconductivity in $WTe_2$ by a proximity effect. *ACS Nano* **12**, 7185–7196 (2018).

[25] Li, Q. *et al.* Proximity-induced superconductivity with subgap anomaly in type II Weyl semi-metal $WTe_2$. *Nano Lett.* **18**, 7962–7968 (2018).

[26] Reeg, C. R. & Maslov, D. L. Hard gap in a normal layer coupled to a superconductor. *Phys. Rev. B* **94**, 020501 (2016).

[27] Nadj-Perge, S. *et al.* Observation of Majorana fermions in ferromagnetic atomic chains on a superconductor. *Science* **346**, 602–607 (2014).

[28] Khestanova, E. *et al.* Unusual suppression of the superconducting energy gap and critical temperature in atomically thin $NbSe_2$. *Nano Lett.* **18**, 2623–2629 (2018).

[29] Li, G., Luican, A. & Andrei, E. Y. Self-navigation of a scanning tunneling microscope tip toward a micron-sized graphene sample. *Rev. Sci. Instrum.* **82**, 073701 (2011).

# Supporting Information: Proximity-induced superconducting gap in the quantum spin Hall edge state of monolayer $WTe_2$

Felix Lüpke[1,*], Dacen Waters[1,*], Sergio C. de la Barrera[1], Michael Widom[1], David G. Mandrus[2,3,4], Jiaqiang Yan[4], Randall M. Feenstra[1], Benjamin M. Hunt[1,†]

[1]Department of Physics, Carnegie Mellon University, Pittsburgh, PA 15213, USA
[2]Department of Materials Science and Engineering, University of Tennessee, Knoxville, TN 37996, USA
[3]Department of Physics and Astronomy, University of Tennessee, Knoxville, TN 37996, USA
[4]Materials Science and Technology Division, Oak Ridge National Laboratory, Oak Ridge, TN 37831, USA
* These authors contributed equally
† E-mail: bmhunt@andrew.cmu.edu

## I Sample fabrication

The newly developed sample fabrication method for the present sample consists of the following steps:

1. Mechanically exfoliate $NbSe_2$ and $WTe_2$ onto $O_2$-plasma-cleaned $SiO_2$ in a nitrogen-filled glove box.

2. Using a PPC/PDMS droplet transfer slide, pick up the $NbSe_2$ flake, then pick up the $WTe_2$ flake. The transfer stage temperature is $\approx 40°C$ for both pick ups.

3. Peel off the PPC layer from the PDMS, flip it upside down and put it onto a second transfer slide which has a PDMS droplet on it into which a hole was cut such that the heterostructure sits close to the center of the hole and does not touch the PDMS.

4. Place the heterostructure onto pre-evaporated gold leads (Au (50 nm)/Pd (30 nm)/Cr (20 nm)) on a $SiO_2$ chip which is mounted on an STM sample plate and wire bonded to contacts sitting the sample plate. Release the PPC by heating it to 100°C.

5. With the sample still at 100°C, remove some of the PPC surrounding the heterostructure using a sharp needle. This step prevents the heterostructure from floating off of the gold lead in the next step.

6. Transfer the sample from the glovebox into vacuum (without exposing it to air), and anneal it at 250°C for 8 h ($p \leq 1 \cdot 10^{-5}$ mBar) to remove the PPC. This step is performed in a tube furnace which has a gate valve and is vented with nitrogen. Subsequently, transfer

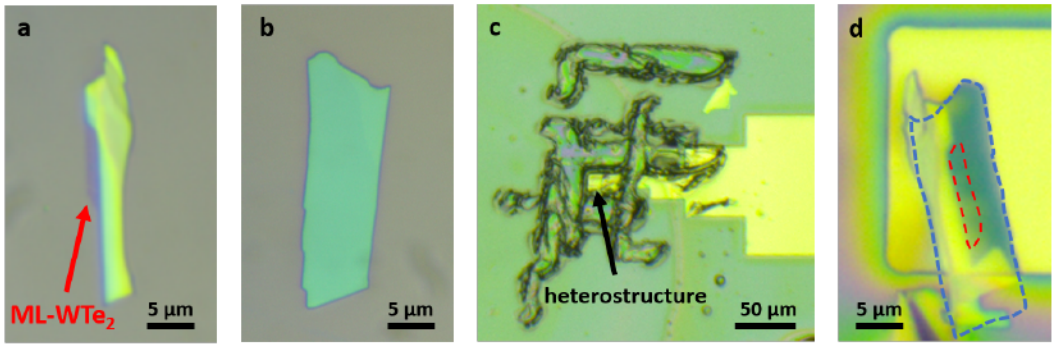


Supplementary Figure S1: Fabrication of the $WTe_2/NbSe_2$ heterostructure. (a), (b) Optical image of the $WTe_2$ and $NbSe_2$ flake after exfoliation onto $SiO_2$. (c) Optical image after putting down the flipped heterostructure onto the gold lead and removing some of the PPC surrounding the flake using a sharp needle. (d) Optical image showing the heterostructure on the gold lead after vacuum annealing. Red and blue dashed lines indicate the outlines of the ML $WTe_2$ and $NbSe_2$ regions, respectively.

the sample to the STM chamber and perform a final annealing step at 250°C for 10 mins ($p \leq 1 \cdot 10^{-8}$ mBar) before putting the sample into the STM.

Using this technique, in contrast to previously reported dry-transfer techniques, the surface of the assembled van der Waals heterostructure is never in contact with any polymer or solvent. This is crucial to achieve an atomically-clean surface. Furthermore, sample fabrication is performed entirely in an inert gas/vacuum environment. This allows to study the pristine surfaces of highly reactive and air-sensitive materials, the only constraint being that the materials do not degrade when annealed at 250°C in vacuum. Supplementary Figure S1 shows optical images of the sample studied in the main text.

## II Moiré effects

Supplementary Figure S2a shows an STM image where both the moiré periodicity and the atomic rows of the ML $WTe_2/NbSe_2$ heterostructure can be seen. Analyzing atomic resolution images of the $WTe_2$ and $NbSe_2$ close to the $WTe_2$ step edge, we find a small rotational misalignment of $\sim 3°$ between the $WTe_2$ $b$-axis and the $NbSe_2$ $b$-axis (Suppl. Fig. S2 (b) and (c)). The resulting moiré period can be approximated as

$$L = \frac{b}{\sqrt{\Theta^2 + \varepsilon^2}} \tag{S1}$$

where $b$ is the $WTe_2$ lattice constant, $\varepsilon$ is its relative lattice mismatch with respect to the $NbSe_2$ ($\sim 1.1\%$) and $\Theta$ is the rotational angle between the two materials [1]. The resulting moiré period is $L \approx 6$ nm which is in good agreement with the periodicity observed in the STM image. Note that the moiré period along the $a$-axis is negligibly small because the rotational misalignment of two $a$-axes is large.

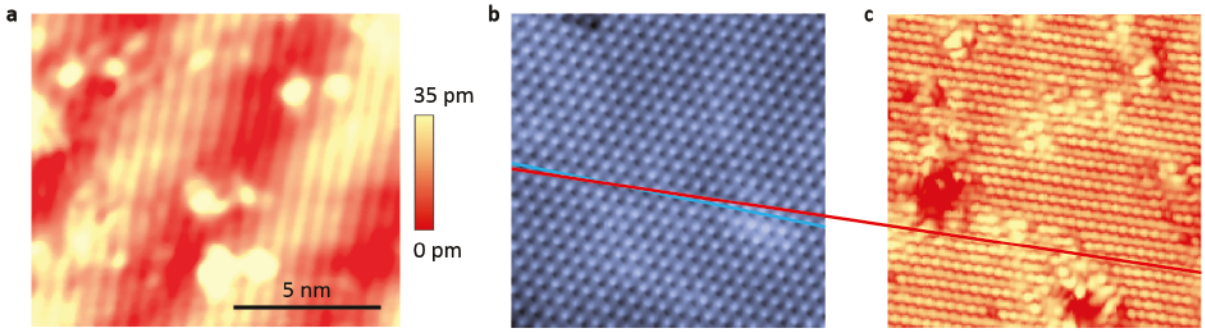


Supplementary Figure S2: a) Topography image of the ML $WTe_2/NbSe_2$ heterostructure, showing the moiré periodicity and atomic rows. The moiré period is $\sim 5\,\mathrm{nm}$ ($V_{\mathrm{sample}} = 1\,\mathrm{V}$ and $I_{\mathrm{t}} = 50\,\mathrm{pA}$). b) Atomic resolution image of $NbSe_2$ right below the step edge of the $WTe_2$. The blue line indicates the orientation of the $NbSe_2$ lattice vector. c) Atomic resolution image of $WTe_2$ right next to the step edge. The red line indicates the orientation of the $WTe_2$ $b$-lattice vector. This misorientation with respect to the $NbSe_2$ is $\sim 3°$.

## III Band gap in ML $WTe_2$

While ARPES [2] and transport measurements [3] show indications of a band gap in the electronic structure of ML $WTe_2$, so far no hard gap has been observed in STM. Among the proposed explanations are defect states or substrate effects [2], a charge density wave [4] and a Coulomb gap [5] which we will discuss below.

Substrate effects may play a role in the observed in-gap conductance in $WTe_2$ grown on epitaxial graphene as well as $WTe_2$ on $NbSe_2$ by tunneling through the $WTe_2$ directly into the underlying layer. In the present sample, if the in-gap conductance would stem predominantly from tunneling into the $NbSe_2$, one would expect to measure the $NbSe_2$ superconducting gap on the ML $WTe_2$. However, we observe a decrease of the superconducting gap as a function of $WTe_2$ thickness which points to the presence of a smaller, proximity-induced, superconducting gap in the $WTe_2$ itself. In an effort to evaluate the possible role of tunneling into $NbSe_2$-derived states for the case of ML $WTe_2$, a separate sample was prepared with the same method described in Section S1, but with an additional layer of $\sim 20\,\mathrm{nm}$ thick hBN underneath the ML $WTe_2$. Optical images of the $WTe_2$ flake after exfoliation and the completed stack with the hBN visible are shown in Suppl. Fig. S3a and b, respectively. Spectra taken in the region indicated in Suppl. Fig. S3b are shown in Fig. 4 of the main text. The spectra on the two different substrates look very similar, but it is immediately noticeable that there is a significant offset in the spectra on the $NbSe_2$. We interpret this as a background in the conductance arising from states associated with the $NbSe_2$ substrate. To quantify the contribution of the $NbSe_2$ to the spectra taken on the $WTe_2$ ML, we compare the value of the conductance at the Fermi energy for spectra on both substrates. We designate this quantity as $A$ in Fig. 4a (ML $WTe_2$ on hBN). For the spectra of the ML $WTe_2$ on $NbSe_2$, $A$ represents the conductance arising solely from the $WTe_2$ while the remainder, $B$ in Fig. 4b, must come from the $NbSe_2$. By comparing spectra at a variety of locations, we find that the fractional contribution to the conductance from the $NbSe_2$

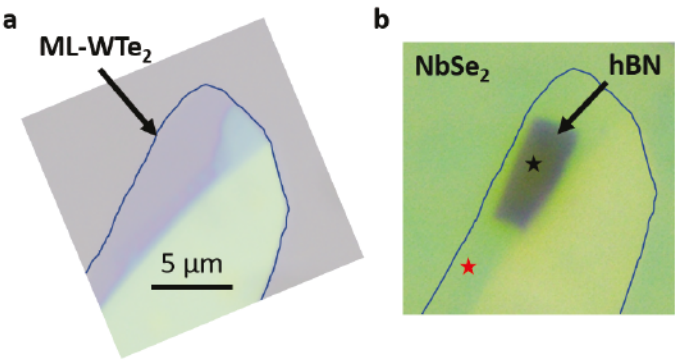


Supplementary Figure S3: (a) A $WTe_2$ flake after exfoliation with the ML region and outline of the flake indicated. (b) Optical image of the assembled $WTe_2$/hBN/$NbSe_2$ heterostructure. The hBN thickness is 20 nm and the $NbSe_2$ is 100 nm. The black and red stars indicate the regions at which spectra were taken in Fig. 4a and b of the main text, respectively.

substrate is $f_{NbSe_2} \equiv B/(A+B) = 0.86 \pm 0.04$ for the measured signal on ML $WTe_2$. While the superconducting substrate does contribute a significant background, the sample prepared on hBN shows that there is still significant non-zero conductance inside the expected band-gap of the ML $WTe_2$, even on an insulating substrate, necessitating another explanation for the in-gap states observed in STS.

By comparing the different STM studies of ML $WTe_2$ [2, 4, 5], defect states seem to be an unlikely explanation because the non-zero $dI/dV$ signal is observed even far away from topographic defects and the observed defect concentration varies.

Another proposed explanation of the observed gap is a charge density wave (CDW) in ML $WTe_2$ [4]. While a CDW may explain the observed gap feature, the doping dependence reported in Ref. 5 does not line up with a typical CDW behavior. Furthermore, the topographic CDW features are not well reproduced in reports other than in Ref. 4. Recently, the gap was proposed to be supported by deformations of the unit cell from a rectangle to a parallelogram at low temperatures [6]. However, in our data we do not observe such deformations, i.e. the angle between the $WTe_2$ lattice vectors is $(90 \pm 1)°$. Lastly, a Coulomb gap due to lateral hopping in the $WTe_2$ ML was proposed as a possible explanation [5]. This explanation is based on ML $WTe_2$ being decoupled from the substrate, which seems reasonable due to the van der Waals stacking and small Fermi surface overlap of the $WTe_2$ ML and graphene as well as $NbSe_2$. To understand the origin of the Coulomb gap in more detail, we consider in the following tip-induced band bending (TIBB) effects.

TIBB can have a significant effect on the measured $dI/dV$ spectra and is known to lead to a finite $dI/dV$ signal in the band gap [7]. The 2D analog of 3D TIBB is a local band shift in the 2D layer. As a result, there is no additional confinement of states in the $z$-direction but only in the $x$-/$y$-plane, i.e. a laterally extended potential well. The depth of the potential well increases with decreasing tip-sample distance and decreasing STM tip work function and results in a local accumulation of charges at the position of the STM tip, i.e. a downward band shift. In the context of TIBB the observed dip in the $dI/dV$ signal at the Fermi energy can be explained

as a Coulomb gap associated with the accumulation layer that is formed in the potential well. TIBB may also explain why the in-gap $dI/dV$ signal and the signature of the Coulomb gap is weak in Ref. 2: in their experiments the current setpoint was much lower (and the work function of their tip may have been higher), producing less TIBB and therefore fewer electrons in the accumulation layer compared to our results and Refs. 4, 5. Furthermore, the presence of a tip-induced electron accumulation layer in the $WTe_2$ can explain the reported conduction and valence band overlap extracted from quasi-particle interference (QPI) measurements in Ref. 5 which is in contrast to ARPES results [2]: with the finite $dI/dV$ signal in the band gap originating from the tip-induced electron accumulation layer, it is expected that the QPI of these states will yield wave vectors corresponding to the down-shifted conduction band states. As a result, QPI is expected to show conduction band wave vectors down to voltages beyond the actual conduction band edge and persist until they are dominated by the valence band conductance. In summary, we believe that TIBB may explain a large part of the range of gap features reported in the literature.

# IV Spectra fitting

The finite-temperature differential conductance function that we fit to the spectroscopic data is the density of states convolved with the derivative of the Fermi function, i.e.

$$\frac{dI}{dV} \propto \int_{-\infty}^{\infty} dE \frac{\exp\left(\frac{E-eV}{k_B T_{\text{tip}}}\right)}{\left[\exp\left(\frac{E-eV}{k_B T_{\text{tip}}}\right)+1\right]^2} N(E) \tag{S2}$$

where $N(E)$ is the density of states of the sample and the density of states in the tip is assumed to be uniform. In standard BCS theory, the density of states $N$ is given by

$$N(E,\Delta) = N_0 \text{Re}\left[\frac{E}{\sqrt{E^2-\Delta^2}}\right] \tag{S3}$$

where $\Delta$ is the gap size of the superconductor and $N_0$ is the normal state density of states, which is typically assumed to be constant. However, in experiments the differential conductance signal often shows a non-trivial normal state conductance around the Fermi energy. To achieve representative fits of the superconducting gaps, we therefore allow for a normal state conductance background given by a low-order polynomial function which we fit simultaneously with the BCS gap function (this is then divided out of the superconducting gap spectra presented in the main text Figs. 2, 3, and 4). We fit the $NbSe_2$ spectra using a two-gap model [8], which we find provides a very good fit at all temperatures. The density of states for the two-gap model is given by

$$N_{\text{NbSe}_2}(E,\Delta_1,\Delta_2) = CN(E,\Delta_1) + (1-C)N(E,\Delta_2) \tag{S4}$$

First, we fit data of Ref. 9 acquired at 100 mK yielding gaps of $\Delta_{\text{NbSe}_2,1} = 1.1844 \pm 0.0021$ meV and $\Delta_{\text{NbSe}_2,2} = 0.8300 \pm 0.0027$ meV (and a tip temperature of $T_{\text{tip}} = 1.0445 \pm 0.0134$ K). The amplitudes of the large-gap and small-gap terms are expressed by parameters $C$ and $(1-C)$, with a value of $C = 0.5424 \pm 0.0047$ found from this fit. This same value of $C$ is then used in fits

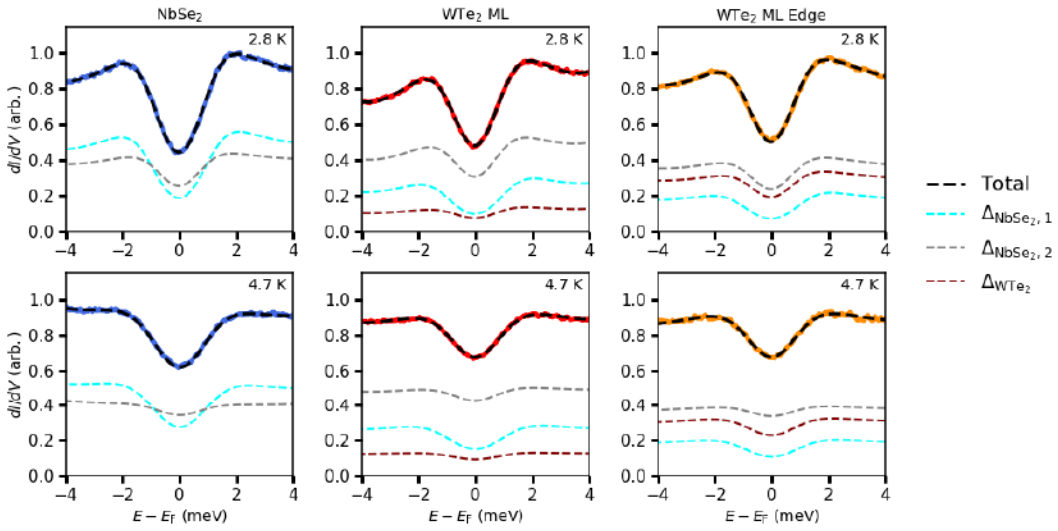


Supplementary Figure S4: Representative raw data differential conductance spectra of $NbSe_2$ (left, blue), $WTe_2$ ML away from the edge (center, red), and $WTe_2$ ML at the edge (right, orange) at STM baseplate temperatures of 2.8 K (top) and 4.7 K (bottom). Best fits of Suppl. eq. S5 are shown as the thick black dashed lines. Thinner dashed lines indicate the relative contribution of each term in Suppl. eq. S5. The vertical scale is the same for each panel. All spectra were taken at $V_{\text{sample}} = 5$ mV, $V_{\text{mod}} = 100$ $\mu$V, $I_{\text{t}} = 100$ pA. In Fig. 4c and d of the main text, the two $NbSe_2$ contribution terms are combined for clarity.

to our own $NbSe_2$ spectra, shown in Suppl. Fig. S4. We find gaps of $\Delta_{NbSe_2,1} = 1.154 \pm 0.031$ meV and $\Delta_{NbSe_2,2} = 0.757 \pm 0.011$ meV with tip temperature of $T_{tip} = 5.962 \pm 0.033$ K at 2.8 K, and gaps of $\Delta_{NbSe_2,1} = 1.051 \pm 0.030$ and $\Delta_{NbSe_2,2} = 0.495 \pm 0.060$ meV with tip temperature of $T_{tip} = 7.405 \pm 0.052$ at 4.7 K. We find that the temperature dependence of the larger of these $NbSe_2$ gap values matches very well to the universal temperature behavior of a BCS superconducting gap. The temperature dependence of the smaller gap does not agree with the universal BCS prediction as well as the large gap behavior, indicating some deviation from the theory. The corresponding sample temperatures in our experiments are approximately 1 K above our measured temperatures STM base plate temperatures.

Moving to the spectra acquired from $WTe_2$ on $NbSe_2$, comparing those spectra to ones acquired from $WTe_2$ on hBN (Fig. 4 of the main text), we see that there is a partial contribution to the measured signal from the underlying $NbSe_2$. We therefore fit our $WTe_2$ spectra with a three-gap model, two gaps of known size from the $NbSe_2$ and one induced gap from the $WTe_2$ whose size is determined from the fit i.e. the density of states is given by

$$N(E) = (1 - f_{NbSe_2})N(E, \Delta_{WTe_2}) + f_{NbSe_2}N_{NbSe_2}(E, \Delta_{NbSe_2,1}, \Delta_{NbSe_2,2}) \tag{S5}$$

We fix the fractional contribution of the $NbSe_2$, $f_{NbSe_2}$, by comparing the value of the observed conductance at the Fermi energy for ML $WTe_2$ on $NbSe_2$ and for ML $WTe_2$ on hBN, as described in the main text. Importantly, for the $NbSe_2$ contribution, the relative amplitudes of the large-gap and small-gap terms is expected to differ from the $C = 0.5424 \pm 0.0047$ deduced above from the bare $NbSe_2$, since the wave functions of the respective states will have varying decay constants as they extend through the $WTe_2$ out into the vacuum. We therefore let $C$ vary in the fits of the $WTe_2$ spectra. The tip temperatures are known from the fits to the bare $NbSe_2$ spectra.

To maximally constrain the fits, we simultaneously fit the spectra acquired at temperatures 2.8 K and 4.7 K, thus having three unknowns in total to fit the two spectra: the induced superconducting gap size for each, and the relative amplitude of the $NbSe_2$ large-gap and small-gap terms (i.e. the same value in both spectra). Using the best fit, midpoint values for all other "auxiliary" parameters ($NbSe_2$ gap sizes, sample temperatures, $WTe_2$ fractional contribution), we find values for the proximity-induced gaps in the $WTe_2$ of $0.80 \pm 0.04$ and $0.73 \pm 0.04$ meV and a fractional magnitude of large-gap term of $C = 0.35 \pm 0.02$, as shown in Suppl. Fig. S4. To properly estimate error bounds for the induced gap, we further perform fits at the minimum and maximum values of the error range of all auxiliary parameters, thus yielding final values for the proximity-induced gaps for ML $WTe_2$ far from an edge of $0.83 \pm 0.08$ and $0.76 \pm 0.16$ meV, along with a fractional magnitude of large-gap $NbSe_2$ term of $C = 0.33 \pm 0.04$. For the case of the $WTe_2$ ML edge on $NbSe_2$, we fit a spectrum acquired at 2.8 K using the known $NbSe_2$ gaps and known tip temperature, with $f_{NbSe_2}$ determined to be $0.65 \pm 0.06$ by comparison of the edge spectrum with those of the non-edge $WTe_2$ on $NbSe_2$ and $WTe_2$ on hBN (we make this indirect comparison because, we cannot measure ML edge spectra on hBN, which would require there to be an exposed (insulating) hBN surface). We fit the edge spectrum using the same fractional magnitude of large-gap $NbSe_2$ term determined from the non-edge spectrum of $C = 0.33 \pm 0.04$. The resulting fit is shown in Suppl. Fig. S4, with induced gap of $0.75 \pm 0.08$ meV. For the case of acquisition temperature 4.7 K, the same procedure yields an induced gap of $0.77 \pm 0.08$ meV.

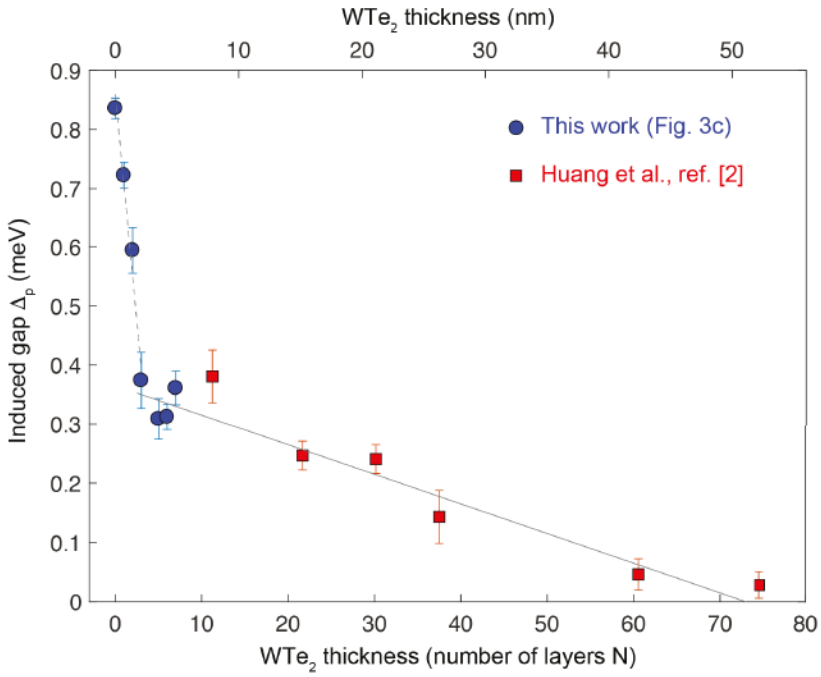


Supplementary Figure S5: Superconducting gap $\Delta_p$ vs. layer number $N$, from Fig. 3c of the main text (blue circles) plotted alongside data extracted from transport measurements in Ref. 10 (red squares). The dashed lines, which are guides to the eye, show the trend of the induced gap in the 'thin' limit ($< 3$ layers) and 'thick' ($\geq 3$ layers) limit. The red data points are calculated by extracting the $\Delta_p/\Delta_0$ values from Fig. 5 in Ref. 10 and multiplying them by $\Delta_0(4.7\,\mathrm{K}) \approx 0.6\,\mathrm{meV}$, a number obtained from Fig. 2g of the same paper. This procedure is valid because the ratio $\Delta_p/\Delta_0$ has a very weak temperature dependence (Fig. 2g of [10]). This allows for direct comparison with our data, which were obtained at 4.7 K.

Let us now consider thicker $WTe_2$ on $NbSe_2$, for which we have measured tunneling spectra at 4.7 K (Fig. 3 in the main text). For three or more layers of $WTe_2$ we fit the observed spectra with a single-gap model (Suppl. eq. S3), obtaining proximity-induced gaps in good agreement with the thickness-trend found in prior measurements of $> 10$ layers of $WTe_2$ on $SiO_2$ [10] as shown in Suppl. Fig. S5. Hence, for three or more $WTe_2$ layers it appears that the contribution of $NbSe_2$ to the observed spectra is negligible. For the case of bilayer $WTe_2$ on $NbSe_2$, there is a sharp deviation from the trend with thickness. must estimate the contribution of the $NbSe_2$ to the spectrum. We have measured a spectrum for bilayer $WTe_2$ on hBN, from which we find the conductance at the Fermi energy to be $1.8\times$ larger than that for $WTe_2$ ML on hBN, thus implying a *lower bound* for the contribution of $WTe_2$ itself to the spectrum of bilayer $WTe_2$ on $NbSe_2$ of $1.8 \times 0.14 = 0.25$. We therefore consider a range of $WTe_2$ fractional contributions for the bilayer case extending from 0.25 to 1.0. For the fractional magnitude of the $NbSe_2$ large-gap term, in the discussion above we found values of $C = 0.54$ and 0.33 for zero and one $WTe_2$ layer, respectively; thus, for two layers of $WTe_2$ we assume values in the range $C = 0.10 - 0.33$. With these parameters, we find a proximity-induced gap for the bilayer $WTe_2$ to be in the range $\Delta = 0.41 - 0.79$ meV, or $0.60 \pm 0.19$ meV. The fit results of the single-gap model for $WTe_2$ thickness greater than the bilayer are reported in Suppl. Table 1.

# V Density Functional Theory Calculations

We performed band structure calculations (Suppl. Fig. S6) using density functional theory (DFT) in the generalized gradient approximation [11] utilizing the projector augmented wave method as implemented in VASP [12]. Lattice constants were set to orthorhombic $WTe_2$ values ($a = 6.249$ Å and $b = 3.477$ Å) for both the ML and the $WTe_2/NbSe_2$ bilayer, while we took $c = 30$ Å to allow sufficient vacuum. Atomic coordinates were relaxed holding the lattice constants fixed prior to calculating the band structure. The results for the freestanding $WTe_2$ monolayer, with and without spin-orbit-coupling (SOC) are shown in Suppl. Fig. S6a and b. Note that in $WTe_2$ the bands near the Fermi energy originate mostly from the W atoms, the orbital character of which we plot as symbols as indicated in the figure legend. The calculations are in excellent agreement with previously reported band structures of 1T'-$WTe_2$. Especially, the inversion of bands with opposite parity is reproduced (marked as "+" and "-" in the figures). Note that the size of the gap, which opens when including SOC into the calculations is under predicted in DFT.

Next, we perform calculations which in addition to the ML $WTe_2$ include a layer of $NbSe_2$ to model the present sample system. For this purpose, we construct a heterostructure unit cell which includes $2\times1$ unit cells of $NbSe_2$ and $1\times1$ unit cells of $WTe_2$. The $NbSe_2$ lattice parameter is adjusted such that the constructed unit cells match in size. We then let the structure relax, before calculating the supercell band structure, with and without SOC. Supplementary Figures S6c and d show the resulting heterostructure bands, where we plot the W orbital character as symbols as before. The $NbSe_2$ bands near the Fermi energy are dominated by Nb which we plot without symbols. From the calculations, we find that the $NbSe_2$ substrate has little effect on the the $WTe_2$ single-particle electronic structure, i.e. we observe no significant band shifts and the band inversion is still present. The Fermi level does shift down by a small amount

| | Parameter | 2.8 K | 4.7 K |
|---|---|---|---|
| $NbSe_2$ | $\Delta_{NbSe_2,1}$ | $1.154 \pm 0.031$ | $1.051 \pm 0.030$ |
| | $\Delta_{NbSe_2,2}$ | $0.757 \pm 0.011$ | $0.495 \pm 0.060$ |
| | $C$ | $0.5424 \pm 0.0047$ (fixed) | |
| | $T_{tip}$ | $5.962 \pm 0.033$ | $7.405 \pm 0.052$ |
| $WTe_2$ ML | $\Delta_{WTe_2}$ | $0.83 \pm 0.08$ | $0.76 \pm 0.16$ |
| | $f_{NbSe_2}$ | $0.86 \pm 0.04$ | |
| | $C$ | $0.33 \pm 0.06$ | |
| $WTe_2$ ML Edge | $\Delta_{WTe_2}$ | $0.75 \pm 0.08$ | $0.77 \pm 0.08$ |
| | $f_{NbSe_2}$ | $0.65 \pm 0.06$ | |
| | $C$ | $0.33 \pm 0.06$ (fixed) | |
| $WTe_2$ bilayer | $\Delta_{WTe_2}$ | | $0.60 \pm 0.19$ |
| | $f_{NbSe_2}$ | $0.25 - 1.00$ | |
| | $C$ | $0.10 - 0.33$ | |
| $WTe_2$ trilayer | $\Delta_{WTe_2}$ | | $0.37 \pm 0.05$ |
| $WTe_2$ five layers | $\Delta_{WTe_2}$ | | $0.31 \pm 0.03$ |
| $WTe_2$ six layers | $\Delta_{WTe_2}$ | | $0.31 \pm 0.02$ |
| $WTe_2$ seven layers | $\Delta_{WTe_2}$ | | $0.36 \pm 0.03$ |

Table 1: Fitting results for key parameters. Details described in Sections S1 and S2. All gap sizes are in meV and all temperatures in K. For the $NbSe_2$ fitting, the value of $C$ in Supple. eq. S4 is fixed by fitting to the data of Ref. [9] taken at 0.1 K. Fractional contribution of $NbSe_2$, $f_{NbSe_2}$, is determined by comparing the $WTe_2$ ML and ML edge spectra on hBN and $NbSe_2$ substrates, as discussed in Section S2, and fixed in each fit of the spectra. 2.8 K data was only taken for the $NbSe_2$ and ML $WTe_2$. Spectra for three or more layers of $WTe_2$ are fit to a single BCS gap model, Suppl. eq. S3 (or equivalently Suppl. eq. S5 with $f_{NbSe_2} = 0$).

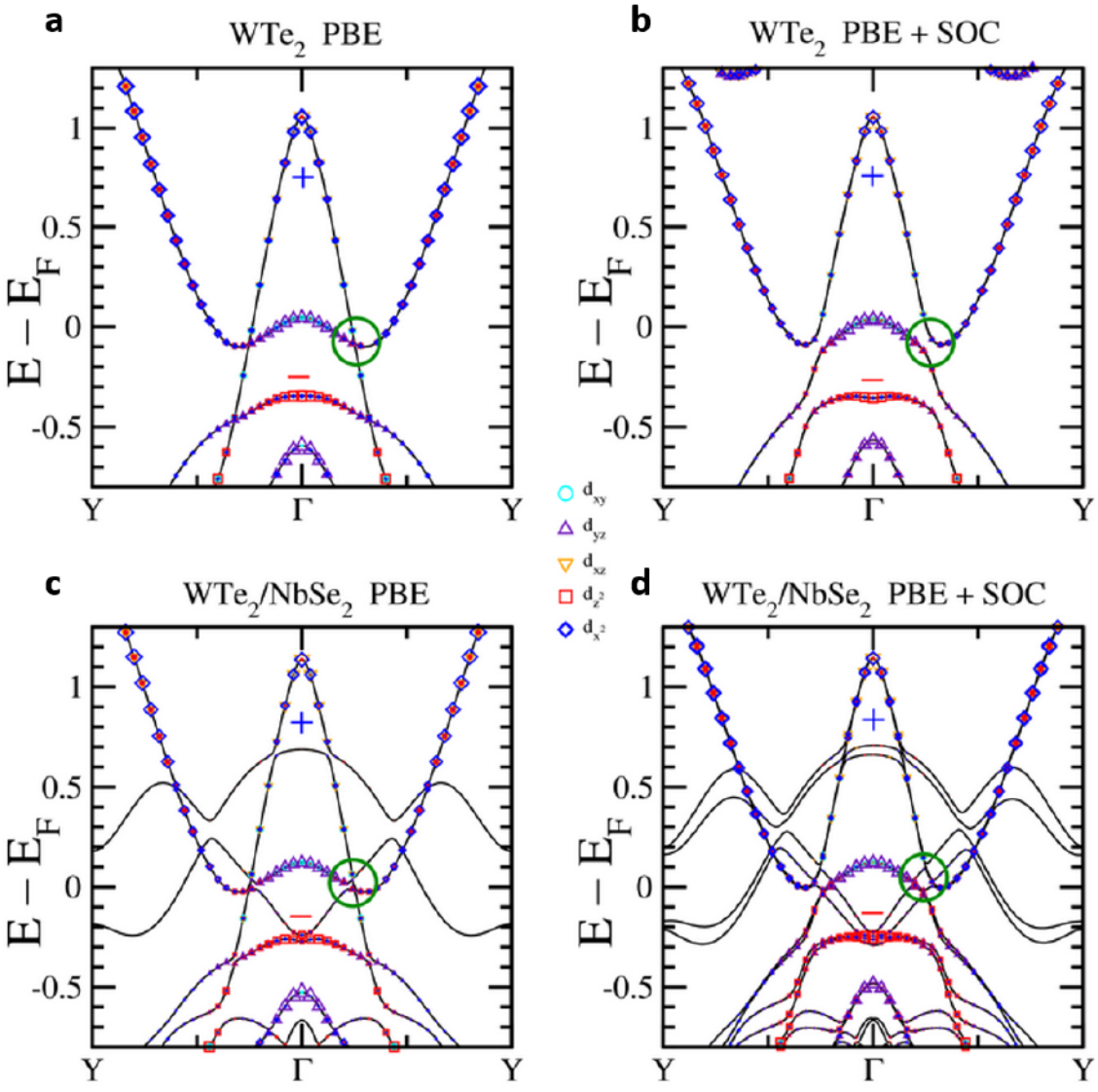


Supplementary Figure S6: DFT band structure calculations showing ML 1T'-$WTe_2$ without spin-orbit coupling (SOC) (a) and with SOC (b). (c) and (d) show the band structure for a heterostructure of ML 1T'-$WTe_2$ and a single layer of 2H-$NbSe_2$, respectively. Calculation details are described in the text. The green circle indicates where SOC forces bands to anti-cross in the pockets along the Y-Γ-Y path for both the ML $WTe_2$ and the heterostructure. The blue + and red − indicates the parity of the states associated with the band inversion necessary for the QSH edge state, in comparison to Fig. 2d and e from Suppl. Ref. [2].

with respect to the conduction band of the $WTe_2$ due to an $NbSe_2$ band near the Fermi energy. Furthermore, we observe hybridization between bands that originate in the $NbSe_2$ and the even parity conduction band of the $WTe_2$, but only at an energy well above the Fermi level. Note that the band splitting in Suppl. Fig. S6d is from the broken inversion symmetry due to the presence of the $NbSe_2$ which lifts the spin degeneracy of the bands when SOC is included. It is worth pointing out that in STM measurements of the $WTe_2/NbSe_2$ heterostructure, we are mostly sensitive to the bands located at the sample surface, i.e. bands of indicated W orbital character. As a results, our tunneling spectra reproduce the bands which look very similar to that of freestanding $WTe_2$. In conclusion, the $WTe_2$ single-particle band structure, including the band inversion and therefore the QSH state, is preserved in a $WTe_2/NbSe_2$ heterostructure.

## Supplementary references


[1] Jung, J., Raoux, A., Qiao, Z. & MacDonald, A. H. Ab initio theory of moiré superlattice bands in layered two-dimensional materials. *Phys. Rev. B* **89**, 205414 (2014).

[2] Tang, S. *et al.* Quantum spin Hall state in monolayer $1T^{'} - WTe_2$. *Nat. Phys.* **13**, 683 (2017).

[3] Wu, S. *et al.* Observation of the quantum spin Hall effect up to 100 Kelvin in a monolayer crystal. *Science* **359**, 76–79 (2018).

[4] Jia, Z.-Y. *et al.* Direct visualization of a two-dimensional topological insulator in the single-layer $1T^{'} - WTe_2$. *Phys. Rev. B* **96**, 041108 (2017).

[5] Song, Y.-H. *et al.* Observation of coulomb gap in the quantum spin Hall candidate single-layer $1T^{'} - WTe_2$. *Nat. Commun.* **9**, 4071 (2018).

[6] Tang, S. Quantum spin Hall state in monolayer $1T^{'}-$TMDCs. In *APS March Meeting 2019, March 4-8, Boston, Massachusetts, USA* (2019).

[7] Feenstra, R. M. Tunneling spectroscopy of the (110) surface of direct-gap III-V semiconductors. *Phys. Rev. B* **50**, 4561–4570 (1994).

[8] Khestanova, E. *et al.* Unusual suppression of the superconducting energy gap and critical temperature in atomically thin $NbSe_2$. *Nano Lett.* **18**, 2623–2629 (2018).

[9] Guillamon, I., Suderow, H., Guinea, F. & Vieira, S. Intrinsic atomic-scale modulations of the superconducting gap of $2h-nbse_2$. *Phys. Rev. B* **77**, 134505 (2008).

[10] Huang, C. *et al.* Inducing strong superconductivity in $WTe_2$ by a proximity effect. *ACS Nano* **12**, 7185–7196 (2018).

[11] Perdew, J. P., Burke, K. & Ernzerhof, M. Generalized gradient approximation made simple. *Phys. Rev. Lett.* **77**, 3865–3868 (1996).

[12] Kresse, G. & Joubert, D. From ultrasoft pseudopotentials to the projector augmented-wave method. *Phys. Rev. B* **59**, 1758–1775 (1999).